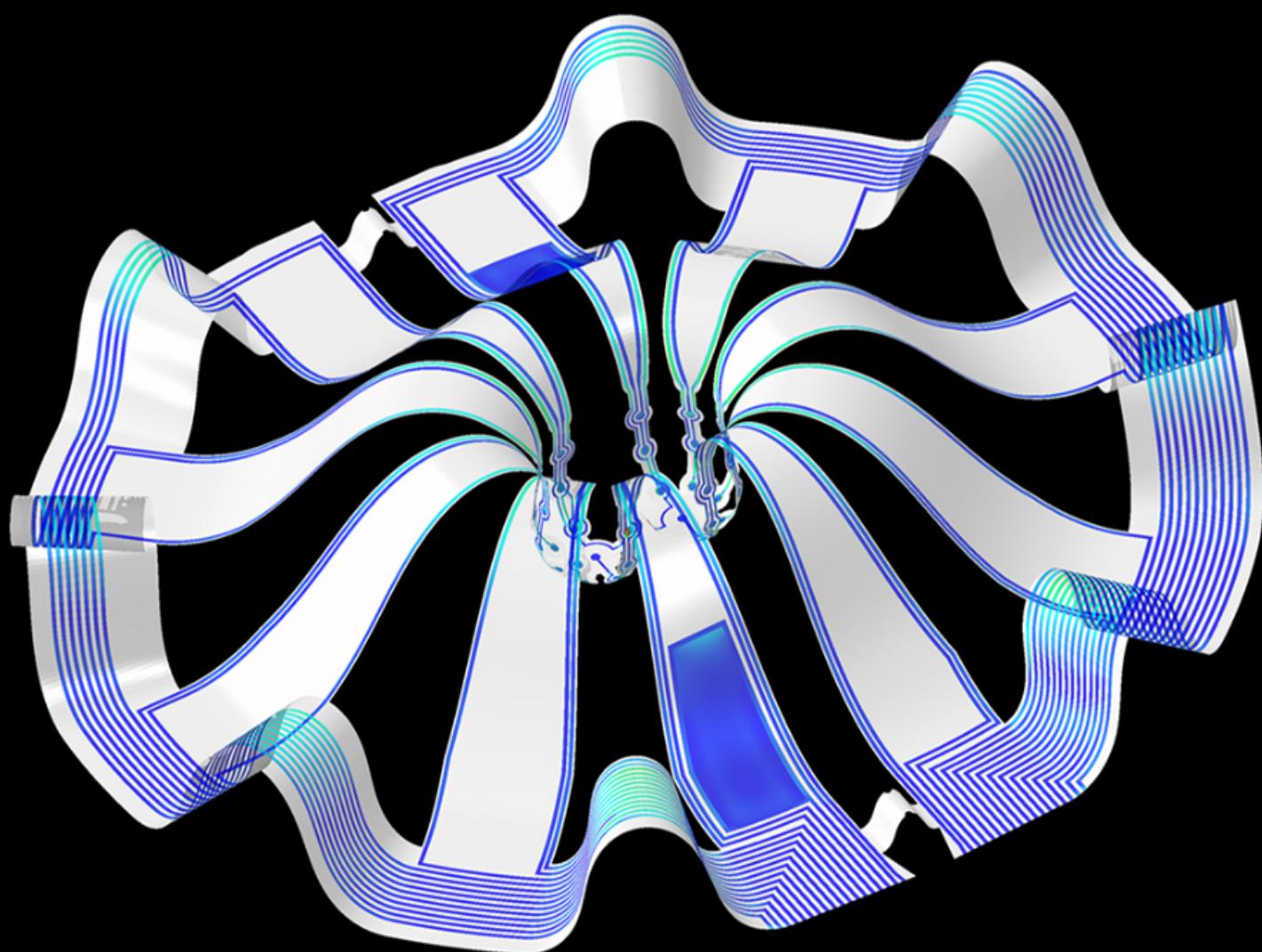APPLIED SCIENCES AND ENGINEERING

Three-dimensional, multifunctional neural interfaces for cortical spheroids and engineered assembloids

Yoonseok Park[1,2]*, Colin K. Franz[3,4,5]*, Hanjun Ryu[1,6]*, Haiwen Luan[1,7,8,9]*, Kristen Y. Cotton[3]*, Jong Uk Kim[1,10], Ted S. Chung[1,11], Shiwei Zhao[7,8,9,12], Abraham Vazquez-Guardado[1,2], Da Som Yang[1], Kan Li[7,8,9,13], Raudel Avila[7,8,9], Jack K. Phillips[14,15], Maria J. Quezada[3,11], Hokyung Jang[16], Sung Soo Kwak[1,6], Sang Min Won[17], Kyeongha Kwon[18], Hyoyoung Jeong[1], Amay J. Bandodkar[1], Mengdi Han[19], Hangbo Zhao[1,20], Gabrielle R. Osher[14], Heling Wang[7,8,9], KunHyuck Lee[1], Yihui Zhang[21], Yonggang Huang[1,7,8,9]†, John D. Finan[14,22]†, John A. Rogers[1,2,7,9,11,23,24,25]†

Three-dimensional (3D), submillimeter-scale constructs of neural cells, known as cortical spheroids, are of rapidly growing importance in biological research because these systems reproduce complex features of the brain in vitro. Despite their great potential for studies of neurodevelopment and neurological disease modeling, 3D living objects cannot be studied easily using conventional approaches to neuromodulation, sensing, and manipulation. Here, we introduce classes of microfabricated 3D frameworks as compliant, multifunctional neural interfaces to spheroids and to assembloids. Electrical, optical, chemical, and thermal interfaces to cortical spheroids demonstrate some of the capabilities. Complex architectures and high-resolution features highlight the design versatility. Detailed studies of the spreading of coordinated bursting events across the surface of an isolated cortical spheroid and of the cascade of processes associated with formation and regrowth of bridging tissues across a pair of such spheroids represent two of the many opportunities in basic neuroscience research enabled by these platforms.

INTRODUCTION

Progress in elucidating the development of the human brain increasingly relies on the use of biosystems produced by three-dimensional (3D) neural cultures, in the form of cortical spheroids, organoids, and assembloids (1–3). Precisely monitoring the physiological properties of these and other types of 3D biosystems, especially their electrophysiological behaviors, promises to enhance our understanding of the interactions associated with development of the nervous system, as well as the evolution and origins of aberrant behaviors and disease states (4–8). Conventional multielectrode array (MEA) technologies exist only in rigid, planar, and 2D formats, thereby limiting their functional interfaces to small areas of 3D cultures, typically confined to regions near the bottom contacting surfaces (9). Optical techniques that use calcium-sensitive fluorescent stains and genetically encoded calcium indicators overcome some of these limitations in neural recording, and optogenetic approaches may

provide related advantages in stimulation. Nevertheless, these methods involve constraints in temporal resolution and in duration of recording across the surface of spheroids/organoids (10–12). An ideal solution would involve soft, shape-matched semiconductor device platforms in 3D geometries that can gently envelop the 3D cultures to support multifunctional electronic, optoelectronic, thermal, mechanical, and biochemical interfaces. Initial work in this direction includes microelectrode shells to wrap individual cardiac cells (13) and cylindrical electrode arrays to contact cardiac spheroids (14). Here, we introduce a qualitatively distinct type of 3D neural interface platform that exploits reversible, engineering control over shapes, sizes, and geometries to match organoids/spheroids of interest, with multimodal engagement. The ability to exploit the most advanced planar electronic and optoelectronic technologies in these platforms represents a key additional unique feature in this context, for high-performance, high-resolution functionality of various types relevant

[1]Querrey Simpson Institute for Bioelectronics, Northwestern University, Evanston, IL 60208, USA. [2]Center for Bio-Integrated Electronics, Northwestern University, Evanston, IL 60208, USA. [3]Regenerative Neurorehabilitation Laboratory, Shirley Ryan AbilityLab, Chicago, IL 60611, USA. [4]Department of Physical Medicine and Rehabilitation, Feinberg School of Medicine, Northwestern University, Chicago, IL 60611, USA. [5]The Ken & Ruth Davee Department of Neurology, Feinberg School of Medicine, Northwestern University, Chicago, IL 60611, USA. [6]School of Advanced Materials Science and Engineering, Sungkyunkwan University (SKKU), Suwon 16419, Republic of Korea. [7]Department of Mechanical Engineering, Northwestern University, Evanston, IL 60208, USA. [8]Department of Civil and Environmental Engineering, Northwestern University, Evanston, IL 60208, USA. [9]Department of Materials Science and Engineering, Northwestern University, Evanston, IL 60208, USA. [10]School of Chemical Engineering, Sungkyunkwan University (SKKU), Suwon 16419, Republic of Korea. [11]Department of Biomedical Engineering, Northwestern University, Evanston, IL 60208, USA. [12]School of Aeronautic Science and Engineering, Beihang University, Beijing 100191, P. R. China. [13]Department of Engineering, University of Cambridge, Cambridge CB2 1PZ, UK. [14]Department of Neurosurgery, NorthShore University HealthSystem, Evanston, IL 60201, USA. [15]Department of Biomedical Engineering, University of Wisconsin-Madison, Madison, WI 53715, USA. [16]Department of Electrical and Computer Engineering, University of Wisconsin-Madison, Madison, WI 53706, USA. [17]Department of Electrical and Computer Engineering, Sungkyunkwan University (SKKU), Suwon 16419, Republic of Korea. [18]School of Electrical Engineering, Korea Advanced Institute of Science and Technology, Daejeon 34141, Republic of Korea. [19]Department of Biomedical Engineering, College of Future Technology, Peking University, Beijing 100871, China. [20]Department of Aerospace and Mechanical Engineering, University of Southern California, Los Angeles, CA 90089, USA. [21]Applied Mechanics Laboratory, Department of Engineering Mechanics; Center for Flexible Electronics Technology, Tsinghua University, Beijing 100084, P. R. China. [22]Department of Mechanical and Industrial Engineering, University of Illinois at Chicago, Chicago, IL 60607, USA. [23]Department of Chemistry, Northwestern University, Evanston, IL 60208, USA. [24]Department of Electrical and Computer Engineering, Northwestern University, Evanston, IL 60208, USA. [25]Department of Neurological Surgery, Feinberg School of Medicine, Northwestern University, Chicago, IL 60611, USA.
*These authors contributed equally to this work.
†Corresponding author. Email: y-huang@northwestern.edu (Y.H.); jdfinan@uic.edu (J.D.F.); jrogers@northwestern.edu (J.A.R.)

to neural interfaces. Complex frameworks as extensions of these concepts offer additional options in precisely and deterministically forming assembloids using spheroids as building blocks. Studies of cortical spheroids formed with human induced pluripotent stem cells (hiPSCs) demonstrate all of the important aspects of this form of 3D neurotechnology.

RESULTS AND DISCUSSION

Figure 1A presents schematic illustrations of a simple, but representative, example designed for a single neural spheroid. This 3D multifunctional framework, which we refer to as a mesostructure because of feature sizes that range from microns to millimeters, follows from techniques of mechanically guided assembly applied to a planar,

lithographically fabricated multilayer stack (see Materials and Methods for details; fig. S1) (15–17) that includes the following: (i) a thin layer of polyimide (PI; PI-2545, HD MicroSystems; 4 μm in thickness) on top; (ii) a network of electrical interconnections and an array of 25 microelectrodes (gold; thickness of 200 nm), with a separately addressable microscale inorganic light-emitting diode (μ-ILED; λ_p = 470 nm; 220 μm by 270 μm; 50 μm in thickness; C470TR2227, Cree), electrochemical sensor, thermal actuator, and precision temperature gauge; (iii) a thin layer of PI (4 μm in thickness) on the bottom; and (iv) a collection of lithographically defined bonding sites (Ti/SiO$_2$; 10/50 nm in thickness) that anchors the system to a soft, silicone elastomeric substrate [poly(dimethylsiloxane) (PDMS), 20:1, Sylgard 184, Dow]. Delivery of this stack onto a prestrained (~30%, equally biaxial) PDMS substrate followed by
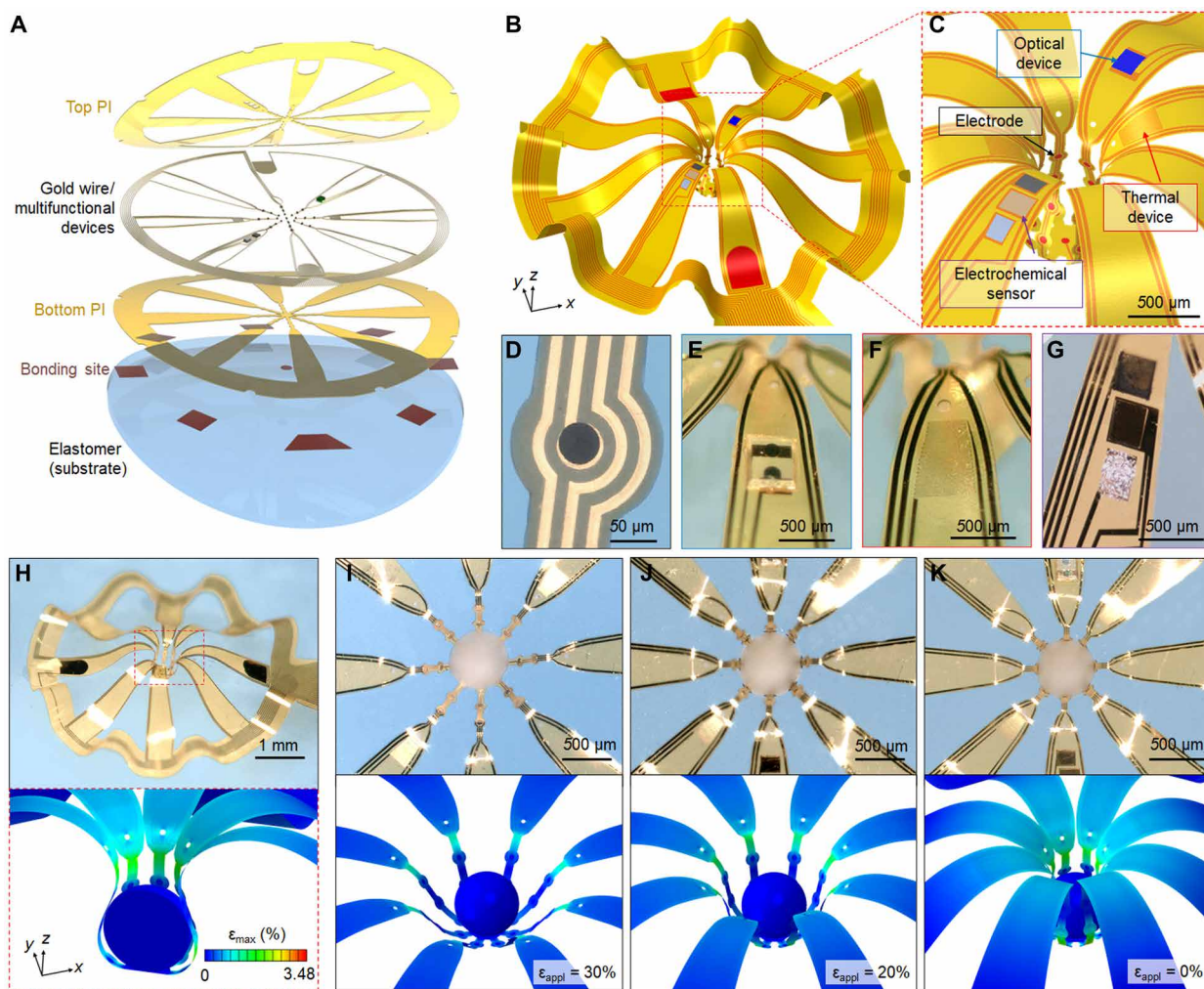

Fig. 1. Schematic illustrations, FEA results, and optical micrographs of a compliant, 3D MMF as an interface to a neural spheroid. (**A**) Tilted exploded view layout of the constituent layers of the 2D precursor to the corresponding 3D MMF. (**B**) Results of FEA of the system in its final configuration and (**C**) a magnified view to highlight the functional components that include 25 microelectrodes, along with devices to provide optical, thermal, and electrochemical capabilities. Optical micrographs of each device, (**D**) circular microelectrode (Pt black, diameter of 50 μm, impedance of 10 kilohms at 1 kHz), (**E**) μ-ILED, (**F**) thermal actuator and sensor (Au trace in a serpentine geometry), and (**G**) electrochemical oxygen sensor (Pt black, Au, and Ag/AgCl as working, counter, and reference electrodes, respectively). (**H**) Optical image of the 3D mesostructure with 25 electrodes and the distributions of maximum principal strain according to FEA across the 3D MMF and the spheroid. Optical micrographs and corresponding FEA results at different stages of the process of enclosing the 3D MMF gently around the surface of the spheroid; from left, (**I**) opening the 3D MMF by stretching the elastomer substrate and placing the spheroid in the center region, (**J**) slowly releasing the substrate to cause the structure to begin to enclose the spheroid, (**K**) completing the release to conclude the integration. Photo credit: Yoonseok Park, Northwestern University.

relaxation of the prestrain leads to compressive forces at the bonding sites that initiate translational and rotational motions in the nonbonded regions, thereby producing the desired 3D structure in a process of controlled, nonlinear buckling (movie S1).

The resulting system (computationally predicted; see the "Procedures for FEA" section in Materials and Methods) in this case consists of a 3D, radially symmetric collection of eight "wings," each with a width of 74 μm along a contour length of 800 μm measured from the point at the center where they connect and bond to the substrate (bonding site of 300 μm in diameter; fig. S2). The width then gradually increases along the length, abruptly at first at a height of 692 μm above the substrate and then more slowly to reach a value of 440 μm at a height of 1.077 mm (the highest point of the structure; lateral distance of 810 μm from the center) and the full width (780 μm) at the end, where the wing bonds to the substrate. These variations in width, together with the thicknesses and bonding locations, define mechanical responses that lead to the desired structural configurations as a result of the 2D to 3D transformation.

Specifically, each wing adopts a 3D shape characterized by concave and then convex bending orientations, changing at a height of 443 μm (38 μm below the third electrode), as the structure moves out of the plane from the center. The bending radii vary gradually from a minimum of 128 μm (concave) near the central bonding site to values of 180 μm (r_{1st}; concave), 267 μm (r_{2nd}; concave), and 252 μm (r_{3rd}; convex) at the first, second, and third electrode locations, respectively, at corresponding heights of 44, 315, and 481 μm (fig. S3A). Circles oriented parallel to the substrate surface and drawn to pass through the first, second, and third electrodes have diameters of 499 μm (D_{1st}), 688 μm (D_{2nd}), and 558 μm (D_{3rd}), respectively (fig. S3). In this way, the overall construct forms a mechanically compliant, pouch-shaped "cage" with an approximately spherical capture cavity designed to hold a single spheroid with a diameter between 480 and 600 μm, without notable deformation/constraint and with sufficient proximity (distances less than ~125 μm, corresponding to roughly half of the average separations between adjacent electrodes) to the electrodes for efficient stimulation and/or recording (fig. S3, C to F).

The bending stiffnesses of the wings that form the cage are exceptionally small, 7.9×10^{-12} N·m², and they increase to 8.3×10^{-11} N·m² at the regions of largest widths (fig. S4A) (as reference, a single strand of silk from an adult silkworm has a bending stiffness of between 10^{-10} and 10^{-11} N·m²) (18). The wings terminate at the bonded locations (bonding areas of 0.78 mm by 0.78 mm) on the substrate, 2.62 mm from the center, to facilitate connection to external electronics for recording and control (fig. S3G). A circular strip of PI with a width of 0.78 mm connects the wings at these locations to ensure stability during the step of transferring the 2D precursors from the source substrate to the PDMS substrate using water-soluble tape. This strip adopts arc-shaped features in between the bonded locations, as a consequence of the 2D to 3D transformation. The peak value (3.48%) of the maximum principal strain (ε_{max}) that arises from the 2D to 3D transformation process occurs at the bottom surface of the PI of the wings near the center, where the bending deformation is the highest. The electrodes and interconnections experience strains less than the yield thresholds of the metal (0.3%), and the PI also remains within its elastic limits (fig. S4, B and C), thereby ensuring reproducibility in the 3D structure formation process and allowing for reversible reconfiguration during insertion and removal of spheroids over hundreds of times (fig. S5).

With these tailored geometric features and low bending stiffnesses, the 3D framework (Fig. 1B) can gently envelop and hold an individual neural spheroid, with additional ability to support multifunctional devices on the individual wings (Fig. 1C). In this example, an electroplated film of nanoporous platinum (Pt black; 4 μm in thickness) on each of the gold microelectrodes ensures a low impedance (~10 kilohms at 1 kHz; Fig. 1D and fig. S6) interface for measurements of local potential. This design feature, together with soft, proximity contacts to the surface of the spheroid, yields high-performance capabilities in recording of neural activity. The blue μ-ILED (λ_p = 470 nm) offers the ability to locally deliver light for optogenetic neural stimulation (Fig. 1E). The serpentine conductive trace (3 μm wide; 200 nm in thickness; 300 ohms in resistance) supports controlled Joule heating for neural inhibition, along with simultaneous measurements of temperature with sub-kelvin precision at a common location (Fig. 1F). An electrochemical sensor that incorporates a gold electrode coated with Pt black, a bare gold electrode, and a silver/silver chloride (Ag/AgCl) electrode as working, counter, and reference electrodes, respectively, allows for monitoring of the concentration of oxygen in culture media immediately adjacent to the corresponding region of the spheroid (Fig. 1G), as a possible indicator of metabolic activity.

Figure 1H shows an optical image of this 3D multifunctional mesoscale framework (3D MMF) with an enclosed spheroid, where 50 contact pads serve as interconnections to external hardware for power supply, control, and data acquisition (fig. S7). Results of finite element analysis (FEA) reveal the distributions of maximum principal strain in both the 3D structure and the spheroid. Such computational approaches allow optimized selection of design parameters to ensure contact with extremely low forces at the soft tissue interfaces. The elastomeric substrate can be reversibly compressed or stretched by small amounts to alter the 3D geometry to accommodate dynamic, natural changes in the size of the spheroid as it evolves and grows. More significant stretching allows the 3D MMF to be opened and closed for inserting and removing the spheroid, all with purely elastic mechanics captured by FEA (Fig. 1, I to K, and movie S2).

A first set of experiments involves preplated hiPSC cortical spheroids (19–21) (10 to 16 weeks old, microBrain, StemoniX; see note S1, figs. S8 and S9A, tables S1 and S2, and Materials and Methods for details), each gently inserted into a 3D MMF according to the procedures outlined above (Fig. 2A). A transparent test platform formed with parylene-C and without microelectrodes or microdevices facilitates imaging by confocal microscopy (22), as in Fig. 2B (note S2). Here, the dashed circles indicate the locations of microelectrodes in an otherwise similar 3D MMF designed for electrophysiological monitoring. The results highlight soft and/or close proximity contacts (separations of less than ~60 μm) to the surfaces of the spheroid, across most (solid angle 3.83π sr; fig. S3, H and I) of its surface area (Fig. 2C), without any noticeable physical damage or deformation of the tissues. Cytotoxicity assay results from enclosed spheroids show no significant differences (P = 0.776) in the viability compared to controls (fig. S9).

Successful recordings of field potentials (Fig. 2E) across each of the 25 low-impedance microelectrodes highlight the high fidelity of the neural interface, at a relevant spatiotemporal resolution (200 μm; 12.5 kHz). Figure 2D and movie S3 highlight representative recordings of the 3D spatial propagation of wave spreading and firing and bursting events across a typical spheroid. Such neuronal bursting is
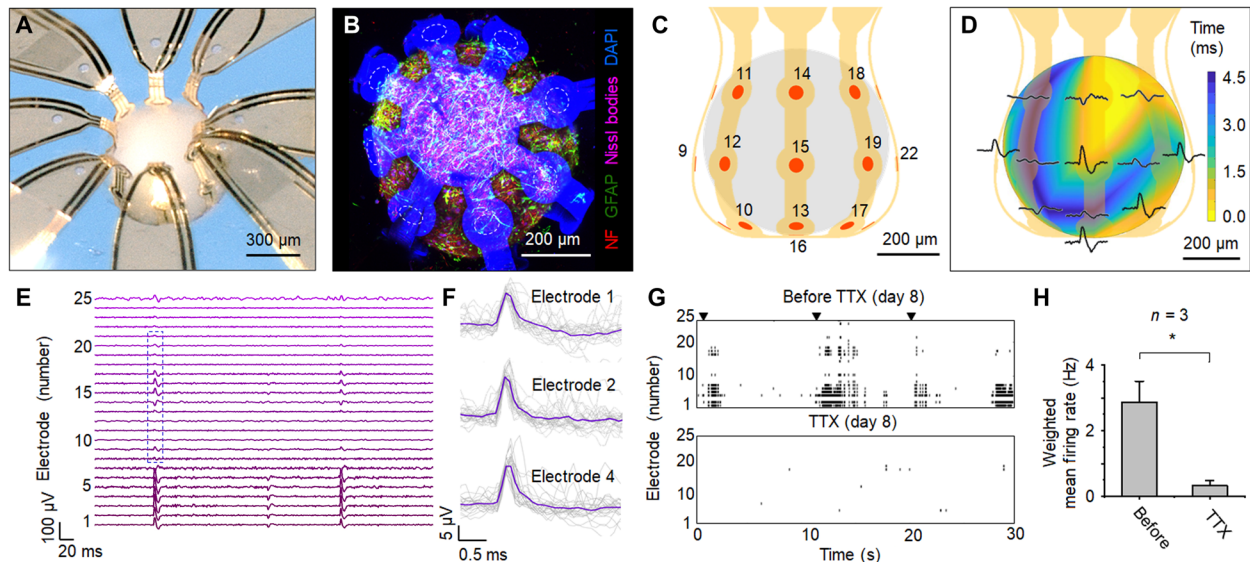
Fig. 2. 3D spatiotemporal mapping of spontaneous neural activity across the surface of a spheroid. (**A**) Optical image of a cortical spheroid enclosed in a 3D MMF designed for electrophysiological recording. (**B**) Confocal microscope image of the spheroid in a similar 3D mesostructure, formed in a transparent polymer (parylene-C) without microelectrodes or interconnections; neurofilament (red), GFAP (green), Nissl bodies (magenta), DAPI nuclear stain (blue), and autofluorescence from the parylene-C (blue). Dashed circles indicate the approximate positions of microelectrodes in a corresponding functional system. (**C**) 3D illustration of the positions of the microelectrodes across the surface of the spheroid. (**D**) 3D plot of time latency associated with traces in the blue box of (E). (**E**) Representative field potentials recorded from all 25 microelectrodes in the system (spheroid 1; table S2). (**F**) Overlaid plots of 30 spikes from channels 1, 2, and 4. Representative spike raster plots (spheroid 3; table S2) (**G**) for network activity of day 8 and suppressed behavior resulting from the application of TTX. (**H**) Weighted mean firing rate (the spike rate multiplied by the number of active electrodes) for representative of 2 min at each condition. $n = 3$ spheroids; *$P < 0.05$; two-tailed paired t test; means ± SEM. Photo credit: Yoonseok Park, Northwestern University.

a common firing pattern of electrical activity observed in many electrophysiological experiments (*9*, *23*) although previously confined to 2D cell cultures and corresponding 2D MEAs. The 3D MMF provides the basis for related studies, but uniquely across the 3D surfaces of spheroids and organoids, of direct relevance to spatiotemporal monitoring of brain activity in the context of diagnosis of brain disease and rehabilitation using clinical electroencephalography (EEG). Figure 2F shows a uniform potential waveform with an average duration of ~0.5 ms and a peak-to-peak amplitude of ~15 μV, characteristic of single-unit action potentials, similar to the waveform observed using reference 2D MEA (Cytoview MEA 6, Axion BioSystems; fig. S10).

Recordings of responses to pharmacological manipulation via applying sodium channel blocker tetrodotoxin (TTX) into the culture media illustrates capabilities in monitoring time dynamic processes. The raster plot before and during TTX (Fig. 2G and fig. S11) shows abolished electrical burst firing during application, qualitatively consistent with expectation. Figure 2H summarizes quantified results of ongoing spiking activity before and during TTX, a significant decrease in the mean firing rate ($P = 0.034$). By comparison to these results, a cortical spheroid placed on a 2D MEA (Cytoview MEA 96, Axion BioSystems) produces signals on only three of the microelectrodes near the base (fig. S10, B and C) due to the strong curvature associated with the spherical shape. This geometrical mismatch prevents meaningful studies related to neural network architectures in these types of 3D systems. The 3D MMF platforms not only solve this challenge, but they also provide other important functional options as described in the following.

Although these and related hiPSC cortical spheroids create many opportunities for in vitro brain studies (*21*), even the most

complex cerebral organoids (*9*) do not yet match the vast anatomic and functional complexity of the adult brain (*24*). Assembly of multiple spheroids (i.e., assembloids) that represent different functional and anatomic domains of the brain is therefore an area of growing interest in research on human brain development and diseases (*25*–*27*). Modeling the migration of neurons and growth of neurites from one region of the assembloid to another is possible, but measuring the functional connectivity represents a major challenge given the constraints inherent to 2D MEAs and related methods. The methods of assembly that form the 3D MMFs of Figs. 1 and 2 (A and B) apply equally well to geometries designed to accommodate multiple spheroids of different sizes and types in various spatial arrangements. An example is a system with 34 microelectrodes designed to mount and support two separate hiPSC cortical spheroids in proximity (17 microelectrodes per spheroid; Fig. 3A). This 3D MMF adopts a shape approximately defined by two overlapping 3D MMFs of the type described for a single spheroid (Fig. 1), but with a total of 10 wings, in two sets of five for each of the two spheroids, connected at the center by a short, arc-shaped ribbon of PI. In this configuration, the structure positions a pair of spheroids at a distance of 550 μm between their centers.

The continuously curved shapes and 3D configurations of the wings are similar to those of the previous example, with bending radii that vary gradually from a minimum of 148 μm (concave) near the central bonding site to a minimum of 358 μm (convex) at a height of 465 μm (fig. S12A) as in Fig. 3B. The maximum height is 1.097 mm, and the diameters are 7.33 and 6.81 mm along the major and minor axes (fig. S12B), respectively. The 34 microelectrodes on these 10 wings allow recording of high-quality field potentials before and during the functional assembly of two cortical
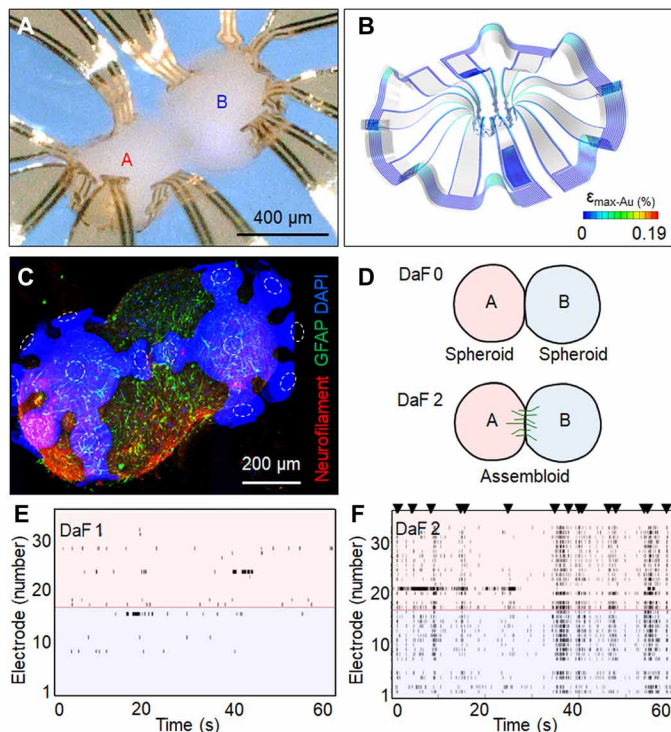
Fig. 3. Optical micrographs, FEA results, schematic illustrations, and electrical measurements associated with a complex 3D MMF designed for the assembly of two neural spheroids into a well-controlled assembloid. (**A**) Optical image of two neural spheroids in a 3D MMF designed to hold them in contact and to measure their neural activity and (**B**) corresponding FEA result (maximum principal strain along the gold wires embedded in PI). (**C**) Confocal microscope image of the two spheroids in a similar 3D MMF formed with a transparent polymer (parylene-C) and without 10 microelectrodes; neurofilament (red), GFAP (green), DAPI nuclear stain (blue), and autofluorescence from the parylene-C (blue). (**D**) Illustration of an assembly of functionally integrated neural spheroids. Raster plots at (**E**) DaF 1 (asynchronous firing) and (**F**) DaF 2 after mounting the two spheroids (assembloid 3; table S2) in this 3D MMF (synchronous firings are indicated using arrow). Photo credit: Yoonseok Park, Northwestern University.

spheroids. The confocal microscope image in Fig. 3C shows the resulting assembloid, along with the form-fitting 3D MMF (autofluorescence arises from the parylene-C).

Detailed studies using this setup reveal interesting processes associated with growth, transection, and regrowth of the neurite bridge between these spheroids, as a model system of neural injury. Figure 3D illustrates the functional assembly between a pair of spheroids using the platform described in the previous paragraph, along with neural activities over 5 days after fusion (DaF; fig. S13) and raster plots for 60 s at DaF 1. These results reveal intermittent firing at all electrodes (Fig. 3E). At DaF 2, the data indicate enhanced activity from each electrode as well as time-synchronized bursting between the two spheroids (Fig. 3F). An experiment that involves electrophysiological recordings before and after transecting the neurite bridge that forms between these two spheroids illustrates processes of neural recovery for a period of days (Fig. 4). The neural activities across both spheroids are synchronous after the formation of the bridge (Fig. 4A, DaF 9). Transection of the bridge on this day does not eliminate firing activity entirely, but the synchrony declines immediately (Fig. 4B, DaF 9). On DaTr 2 (day after

transection), the neurite bridge reestablishes, and synchronous firing resumes (Fig. 4C) with time frames similar to those associated with the initial formation of the bridge (2 days; fig. S14). Figure 4 (E and F) shows quantified results of ongoing spiking activity (synchrony index, mean firing rate) before and after transection. While the mean firing rates return to baseline on DaTr 2, the electrophysiological pattern underlying this recovery is unexpectedly heterogeneous. Figure 4G shows that the early reduction in mean firing rate on DaTr 0 is mainly driven by the large (>25%) decrease in spontaneous activity recorded in the subgroup of electrodes (dot patterned) across the assembloid rather than a global depression within each spheroid. The recovery at 48 hours (DaTr 2) leads to an increased proportion of electrodes showing enhanced spontaneous activity compared to baseline (diagonal stripes, wide downward patterned) rather than a uniform recovery across each electrode. The transection model presented here reproduces neurite neural injury and recovery in a 3D human system and provides direct electrical evidence of functional reintegration. Future studies using anatomic techniques such as neuron tracing may be incorporated into this model to define how different repair processes contribute to the recovery process (e.g., axon regeneration versus collateral sprouting).

In all of these and other cases, a heterogeneous collection of device components can be integrated into the 3D MMF for multifunctional capabilities beyond electrophysiological mapping. Individual devices can provide useful, multifunctional forms of neuromodulation in precisely controlled locations across the 3D MMF, thereby providing a constant condition to interact with the spheroid during stimulation and measurement. The system in Fig. 1 (C to G) includes an optical device (blue μ-ILED, λ_p = 470 nm), thermal actuator, electrochemical oxygen sensor, and low-impedance electrodes for both recording and electrical stimulation. These functions, especially those in neuromodulation (28), allow the use of the 3D MMF as a microlab for investigating various induced and natural behaviors of organoids.

Electrically evoked neural activity in spheroids, for example, can be important in assessing circuit formation and neuron intrinsic properties, as a possible correlate to clinical EEG diagnostic studies and therapeutic brain stimulation (29, 30). The plots in Fig. 5 (A to D) show field potentials on a neural spheroid evoked at a single electrode (number 19) with an applied 5-μs voltage pulses (V_{app}) of 5 mV (Fig. 5B), 10 mV (Fig. 5C), and 50 mV (Fig. 5D). The amplitude of the field potential increases from 0.3 mV (V_{app} = 5 mV) to 1.3 mV (V_{app} = 50 mV), and the number of microelectrodes that respond to the electrical stimulation increases from adjacent 6 electrodes (total of 13 including backside) to all of 24 electrodes with a stimulation voltage (fig. S15) similar to previously reported in vivo electrode systems EEG and fluorescence imaging (31). Microscale focal stimulation (~250 μm in diameter) is hard to achieve without conformal contact between electrode and tissue in vitro and in vivo. The finding shows that focal neural modulation of the brain in vitro is possible through the 3D MMF, with high spatial resolution. Study opportunities include electrically modulated seizures or epilepsy suppression (32) using brain organoids.

Activating the blue μ-ILED exposes the neural spheroid (fig. S16) to localized illumination at a well-defined intensity, as shown in Fig. 5E (3D computational results). Optogenetic control of hiPSC cortical spheroids is achieved 7 to 10 days after transfection (33) with representative field potential traces (see Materials and Methods for detail; fig. S17 and note S3). The integrated electrochemical
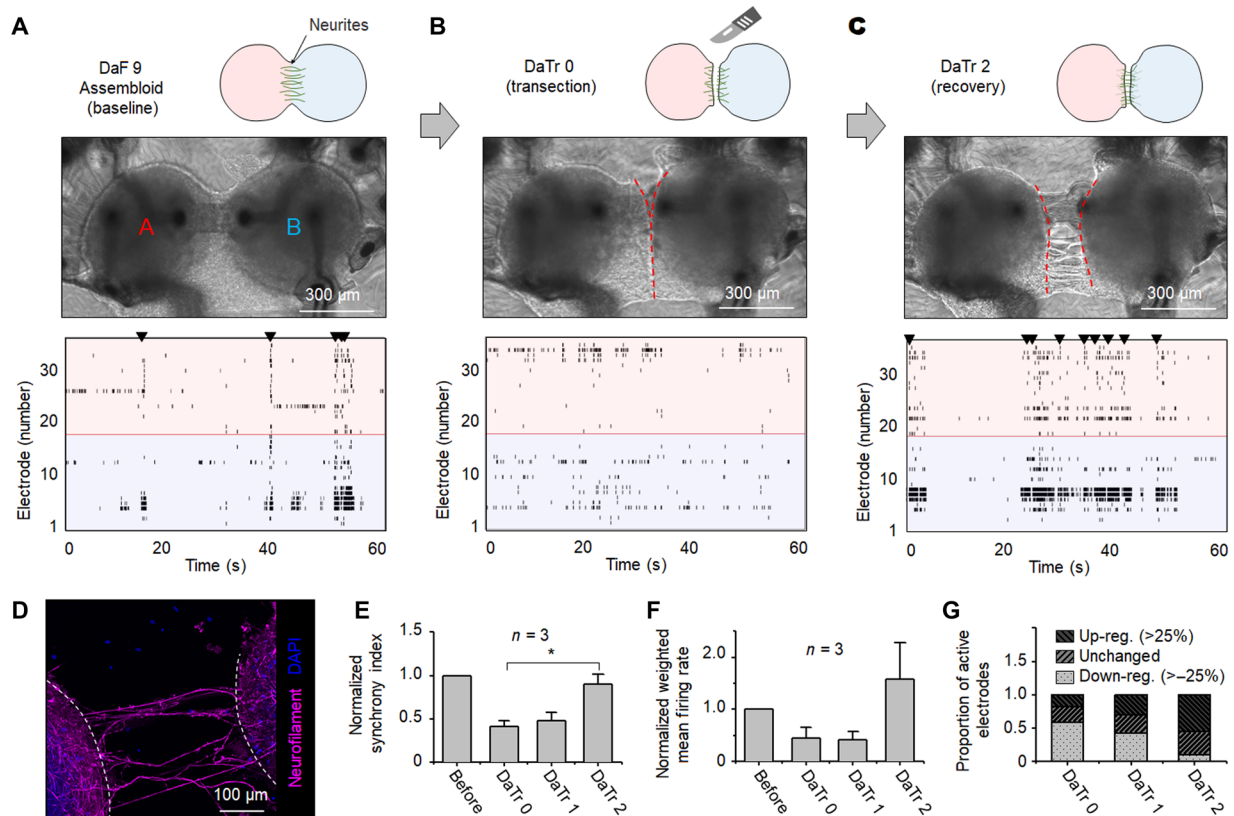
Fig. 4. Schematic illustrations, optical micrographs, and 3D measurements of neural activity associated with transection and neural recovery of a neurite bridge in an assembloid. Illustrations, optical images, and raster plots (**A**) before and (**B**) after transection of the neurite bridge that joins the spheroids of this assembloid on 0 DaTr and (**C**) recovery after transection on 2 DaTr. (**D**) Confocal microscope image of the neurite bridge that formed between the spheroids of an assembloid stained with neurofilament (violet) and DAPI nuclear stain (blue). (**E**) Quantification of the synchrony index over 2 days and (**F**) weighted mean firing rate before, after transection, and recovery (recording time $n1 = 10$, $n2 = 4$, and $n3 = 20$ min). $n = 3$ spheroids; *$P < 0.05$; one-way repeated-measures analysis of variance (ANOVA) followed by Tukey test; means ± SEM. (**G**) Up- and down-regulated mean firing rate after transection on DaTr 0, 1, and 2.

oxygen sensor can capture the concentration of oxygen in culture media adjacent to the spheroid, with levels of accuracy that compare favorably to those of conventional commercial devices (fig. S18).

Another enablement is in the study of the effects of hyperthermia and associated depression of cortical activity (*34*), relevant to modeling various stressors from thermal and toxic to neurodegenerative disease (*35*, *36*). Here, the thermal actuator (gold wire; thickness of 200 nm; width of 3 μm; resistance of 300 ohms) provides finely controlled levels of heat stress to temperatures up to 50°C and with possibilities for control of the set point temperature to a precision of a few tenth of a degree. A pair of conductive traces in serpentine geometries serves as a thermal actuator and a temperature sensor, for closed-feedback loop control (fig. S19). The spatial distribution of temperature around and within the spheroid can be captured by 3D computational modeling, as in Fig. 5F. The raster plot in Fig. 5G shows that a relatively brief exposure to elevated temperature (43°C; local temperature onto the surface of spheroid adjoining to thermal actuator, $\Delta T = 6$°C; 5 min) reversibly suppresses network bursts measured simultaneously with the electrode array. Rapid recovery of activity, after 5 min, occurs following deactivation of the thermal actuator, as the temperature returns to its baseline value (37°C). The actuator provides a constant 43°C heat stress over approximately half of the spheroid (~39°C opposite half), leading to focal

up-regulation of heat shock protein 70/72 (HSP70/72) only over this side (HSP70, indicated as green; Fig. 5H).

The 3D MMF systems introduced here offer features such as geometry, size, and component configuration that scale naturally, where FEA (*16*, *17*) serves as a versatile design tool not only for the architectural parameters but also for the various modes of operation. The results create opportunities for assembly of various spheroids/organoids from different domains of the central, autonomic, and peripheral nervous systems in different shapes and sizes, in complex configurations and even as 2D arrays of 3D MMFs with different layouts and functions. Figure 6A presents an example of a 3D MMF with a layout that accommodates three spheroids to form an assembloid with a triangular lattice geometry, approximately characterized by a partial overlap of three 3D MMFs designed for single spheroids (Fig. 1), where each with four wings encloses roughly half of the surface area of each spheroid. The structure defines distances of 550 μm between the centers of the spheroids, with 12 wings that create a mesoscale cage to enclose three 580-μm spheroids with soft contact (bottom left in Fig. 6A and fig. S20A). The maximum height and the diameter are 1.049 and ~0.847 mm (fig. S21A), respectively, with designs that ensure that the material strains remain in the elastic response regime during the 2D to 3D transformation (Fig. 6A). Extensions to assembloids that include larger collections of spheroids
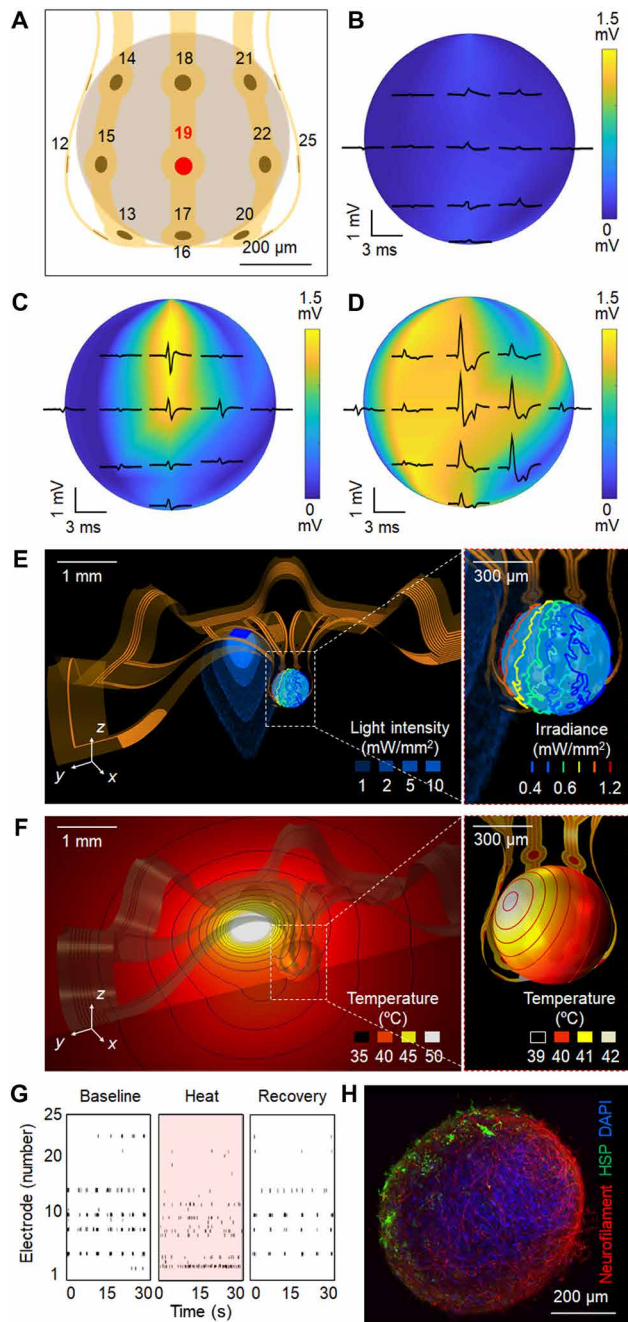
Fig. 5. Results of multimodal stimulation and recordings from cortical spheroids using 3D MMFs. (**A**) 3D map of 12 microelectrodes surrounding a stimulation electrode (number 19). 3D plot of the amplitude of field potentials on the neural spheroid evoked by biasing this electrode to potentials of (**B**) 5 mV, (**C**) 10 mV, and (**D**) 50 mV. (**E**) Computed 3D spatial distribution of light intensity across the culture media and surface of a neural spheroid induced by illumination from a μ-ILED integrated into the 3D MMF. (**F**) Computed 3D spatial distribution of temperature across the culture media and surface of a neural spheroid induced by a thermal actuator integrated into the 3D MMF. (**G**) Raster plot of spiking activity associated with baseline behavior (before heating), 5 min exposure to thermal stress at 43°C (ΔT = 6°C), and after return to baseline. (**H**) Confocal microscope image of focal heat shock response on the spheroid associated with heating for 1 hour by a thermal actuator (43°C). The pattern of HSP70 staining corresponds to a region where heat shock applied; neurofilament (red), HSP70 (green), and DAPI nuclear stain (blue).

in planar geometries are straightforward, and 3D configurations may also be possible.

As another option, the 2D precursor structures can be formed in separated multilayers such that the mechanical 3D assembly process yields not only a curved framework to support a spheroid from the bottom but also a matching top capping structure that supports additional microelectrodes, for full coverage across the entire 4π solid angle, as in Fig. 6B. Here, 3D transformation of the top and bottom 3D structures creates a "full spherical cage" with an approximate diameter of 580 μm (Fig. 6B). The maximum height and diameter are 0.580 and 1.565 mm (fig. S20B), respectively, with other geometrical details in figs. S3 and S21A. An additional example of design versatility is in 3D MMF structures with deformable, serpentine structural elements (Fig. 6C) to allow for mechanical deformations that can follow natural variability in the sizes of the organoids during neural development and growth. As an example, a radially symmetric collection of six wings combined with serpentine elements yields a 3D stretchable cage at the center, with an outer diameter of ~650 μm at the widest point for a spheroid with a diameter of 575 μm (fig. S20C). The deformable space can expand easily and reversibly to an outer diameter of ~700 μm (with PI thickness of 3 μm), suitable for a spheroid with a diameter of 650 μm (Fig. 6C).

As mentioned previously, the most advanced 2D lithographic techniques, thin film growth and etching methods, and other forms of processing from the semiconductor industry can be leveraged for the functional elements. For instance, photolithographic patterning can provide high-density arrays of microelectrodes with sizes comparable to individual neurons (nine electrodes in 60 μm by 60 μm; electrode size of 10 μm; distance between electrodes of 30 μm; fig. S22), for enhanced spatial resolution relative to previously described examples. The parallel nature of these processes and the 3D assembly techniques allow immediate access to large arrays of 3D MMFs, of interest for high-throughput screening and/or statistical studies on various types of organoids. Examples in Fig. 6 show 3D MMFs with different characteristic dimensions (from left, spherical "cages" for spheroids with diameters of 600, 720, and 900 μm; Fig. 6D) and in a 4 × 4 array (16 3D MMFs for spheroids with diameters of 600 μm; Fig. 6E and fig. S23).

The work reported here establishes a versatile 3D neural interface with unique capabilities in fundamental studies of spheroids, organoids, and assembloids. Such culture systems have already contributed much to our understanding of neurodevelopmental disorders, such as microcephaly (*37–39*) and neurodegenerative disorders such as Parkinson's (*40*) and Alzheimer's disease (*41*). Most neurological disorders arise, however, from abnormal function in brains with grossly normal structures. Organoids and assembloids have the potential to reproduce these functional abnormalities (*25, 42, 43*), and the 3D neurotechnology platform introduced here will harness that potential with greater detail and efficiency than can be realized using conventional methodologies. Integrated light sources can evoke activity in a single, genetically modified cell type in a coculture of many types. Heating elements can create spatially heterogeneous patterns of thermal stress that can be superimposed on the spatially heterogeneous cellular and regional identity of a culture. Arrays of microelectrodes across the 3D culture can evoke and/or quantify electrophysiological network phenotypes across all these scenarios. Additional opportunities will follow from 3D integration of microelectromechanical systems for force actuation and measurement, microfluidic networks for delivery of pharmaceutical agents and
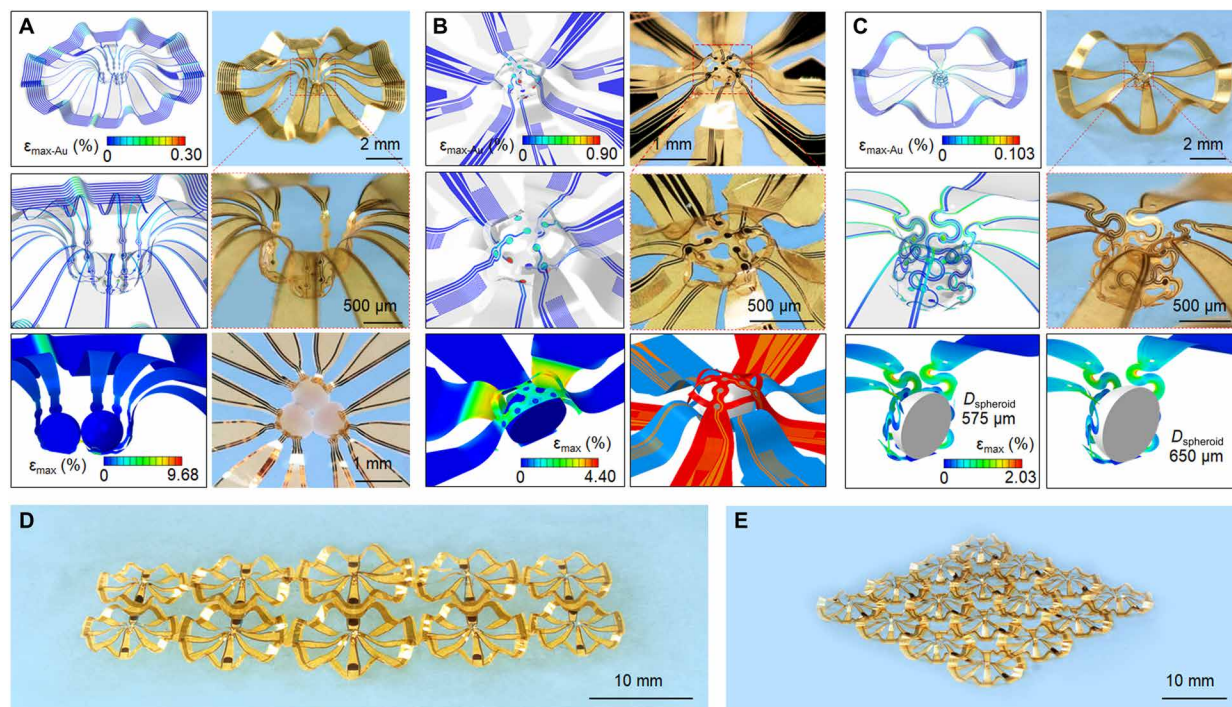
Fig. 6. 3D MMFs with advanced features, as isolated units and arrays. (**A**) FEA results and optical micrographs of a 3D MMF designed to create assembloids of three spheroids in a triangular lattice geometry. (**B**) 3D MMF with full coverage across an entire 4π solid angle. (**C**) 3D MMF with serpentine wires designed to stretch and deform to accommodate volumetric growth of an inserted spheroid. Arrays of these and other 3D MMFs are of interest for high throughput screening and/or size selection, (**D**) with the same or different characteristic dimensions, (**E**) with ability to for simultaneous monitoring of up to 16 spheroids. Photo credit: Yoonseok Park, Northwestern University.

sampling of adjacent fluids, biochemical sensors for monitoring the transport of biomarkers to and from tissue surfaces, scaffolds for improving nutrient perfusion to maintain deep cells, and penetrating, multifunctional probes for interfacing to targeted depths beneath these surfaces where fundamental neural dynamics occur. The breadth of options suggests great promise for the use of these 3D MMFs in wide-ranging programs of research in modern neuroscience.

MATERIALS AND METHODS
Fabrication of the 3D MMF
Preparation of 2D precursors began with spin coating (3000 rpm for 30 s) and curing (180°C for 2 min) a thin layer of poly(methylmethacrylate) (PMMA) on a clean glass slide, followed by spin coating and fully curing (260°C for 1 hour) a layer of PI (4 μm; PI-2545, HD MicroSystems). Electron beam evaporation formed thin films of chrome (Cr, 10 nm) and gold (Au, 200 nm) on the PI. Photolithography and wet etching yielded patterns of interconnections and microelectrodes. Spin coating and curing another layer of PI (4 μm) created an insulating film on these conductive features. A thin layer of copper (Cu, 50 nm) deposited on the PI by sputtering and patterned by photolithography and wet etching served as a hard mask for oxygen plasma etching (220 mT, 200 W, 50 min) of the exposed regions of the PI. Immersion in acetone overnight dissolved the underlying PMMA, thereby allowing the structures to be retrieved from the glass slide. Transferring this 2D precursor onto the surface of a water-soluble polyvinyl alcohol (PVA) tape allowed for deposition of Ti/SiO_2 (10 nm/50 nm in thickness) via electron beam evaporation through a shadow mask onto the back side to define bonding sites. Exposing the 2D precursors and the surface of an elastomer

substrate (≈1.5-mm sheet of PDMS) to ultraviolet (UV)–induced ozone generated surface hydroxyl groups to facilitate covalent linkages at the positions of the bonding sites. Prestretching the elastomer to an equal biaxial strain of 30%, laminating the 2D precursors/PVA tape on top, and heating to 70°C for 10 min led to strong bonding, dissolving the PVA frameworks via processes of mechanical buckling. A polystyrene petri dish (Thermo Fisher Scientific, MA, USA; 35 mm in diameter, 10 mm in height) with an opening (2 mm in diameter) in the bottom was mounted on the PDMS substrate using silicone adhesive (Kwik-Sil, World Precision Instruments Inc., FL, USA). Illustrations in fig. S1 show each step in detail.

Electrochemical deposition of Pt black and measurements of impedance
Platinum black was deposited by chronoamperometry (−0.1 V for 20 s) using a three-electrode system (Autolab PGSTAT128N, Metrohm AG, Switzerland) with a Pt wire for the counter electrode and Ag/AgCl for the reference electrode, in a mixture of 3 weight % (wt %) chloroplatinic acid ($PtCl_6H_2$; Sigma-Aldrich, MO, USA) and 0.1 wt % lead acetate [$Pb(C_2H_3O_2)_2$; Sigma-Aldrich, MO, USA]. Measurements of the impedance at frequencies between 1 Hz and 10 kHz in a solution of phosphate-buffered saline (PBS; pH 7.4) relied on a commercial analyzer (Autolab PGSTAT128N). A schematic illustration of the setup is in fig. S6E.

Integration of the μ-ILED
Applying small amounts of silver epoxy (8331 Silver Adhesive; MG Chemicals, BC, Canada) on the anode and cathode regions of the μ-ILED ($λ_p$ = 470 nm; 220 μm by 270 μm; thickness of 50 μm; C470TR2227, Cree, NC, USA) prepared the devices for integration

onto corresponding electrode pads on the 2D precursor by transfer printing. Spin coating and curing (250°C for 2 hours) yielded a conformal dielectric layer of PI over the μ-ILED for encapsulation. Optical measurements of the light output were performed with a digital power meter (PM100D, power meter and S120VC, photodiode sensor, Thorlabs, NJ, USA). Illustrations in fig. S16 show each step in detail.

Fabrication of the electrochemical sensor

The electrochemical sensor incorporated three electrodes: working, counter, and reference. Electroplating porous Pt on a gold electrode (250 μm by 300 μm) formed the working electrode. Laminating Ag/AgCl paste on a different gold electrode (250 μm by 300 μm) formed the reference electrode. A bare gold electrode served as the counter electrode. Illustrations in fig. S18 show each step in detail.

Formation of hiPSC-derived 3D cortical neuron/astrocyte cocultures

Preplated 3D human cortical neural spheroidal cocultures were provided by StemoniX Inc., in the form of the StemoniX microBrain 3D Assay Ready product (StemoniX, MN, USA). Each well of the plate contained a single, free-floating hiPSC-derived cortical 3D neural cell culture generated from neural progenitor cells obtained from a single human donor source. StemoniX shipped the microBrain 3D Assay Ready plates overnight under ambient conditions. Upon receipt, plates were processed according to the detailed instructions provided. Briefly, after unpacking, the plates were centrifuged for 2 min at 200g (Sorvall centrifuge) and then inspected using a light microscope to ensure the presence of a single spheroid in each well. Plate exteriors were decontaminated with 70% ethanol. After unsealing, the medium was changed (1/2 volume, three times) using the BrainPhys Neuronal Medium SM1 Kit (STEMCELL Technologies, no. 05792, BC, Canada) supplemented with recombinant human brain-derived neurotrophic factor (20 ng/ml; STEMCELL Technologies, no. 78005, BC, Canada), glial cell line–derived neurotrophic factor (20 ng/ml; STEMCELL Technologies, no. 78058, BC, Canada), and 1× penicillin-streptomycin (GE Healthcare Life Sciences, PA, USA) or the NeuralX Cortical Neuron media kit that follows a recipe published by Bardy et al. (44) (StemoniX, NXCNM-AA-0250, MN, USA). Spheroids were maintained at 37°C and 5% CO_2 until used in experiments. Half media changes were performed Monday, Wednesday, and Friday using one of the two media described above, which are interchangeable according to the manufacturer's instructions.

Insertion of cortical spheroids into the 3D MMF

The petri dish with 3D MMF was sterilized by UV light illumination for 30 min and subsequent soaking in 70% ethanol solution and three washes with PBS (1×; Thermo Fisher Scientific, MA, USA; catalog no. 10010023) for 15 and 5 min, respectively. Opening of the 3D MMF began with dropping the media (two to three drops) around the 3D MMF in a petri dish, gently pressing the bottom of the PDMS substrate (2 to 3 mm vertically). Collecting spheroids from each well of the plate was performed by firmly pipetting (with a wide-bore P200 tip) the medium in the well and transferring it onto 2D semitransformed MMF. After placing the cortical spheroid onto the 3D MMF, releasing the PDMS substrate transformed the 2D MMF into 3D MMF and enclosed the spheroid. The petri dish was filled with media and maintained at 37°C and 5% CO_2. The enclosed spheroids were stained for neurofilament heavy chain

(NF, Abcam, Cambridge, UK, ab72996), glial fibrillary acidic protein (GFAP; DSHB, Hybridoma product 8-1E7, IA, USA), Nissl bodies (Invitrogen, N21482, CA, USA,), and 4′,6-diamidino-2-phenylindole (DAPI; Invitrogen, D1306, CA, USA) and imaged with confocal microscopy.

Acquisition of electrophysiological data

A commercial system (Maestro Pro, Axion Biosystems, GA, USA) and its companion software (Axion Biosystems Integrated Studio, AxIS) served as the basis for collection and, in some cases, analysis of electrophysiological data. The system recorded from all electrodes simultaneously with a sampling rate of 12.5 kHz and real-time display capabilities. Data collection used the neural spike setting, with a gain of 1000× and a bandpass filter between 200 Hz and 4 kHz. The AxIS software labels spikes as signals with amplitudes above a threshold of 6 SDs from the average noise level; bursts as a minimum of five spikes with a maximum interspike interval of 100 ms; network bursts as a minimum of 50 spikes from at least 35% of the electrodes with a maximum interspike interval of 100 ms; and the synchrony index by first taking the cross-correlation between all the pairs of spiking electrodes over a 20-ms window, removing the autocorrelations, and then running it through a kernel to get a single metric, where 1 is perfect synchrony and 0 is no synchrony.

Preparation of spheroids for optogenetic studies

We generated high-titer lentiviruses [109 to 1010 transduction units (TU)/ml] to express a blue light–activated channelrhodopsin actuator known as CheRiff-EGFP (Addgene #51693), under the control of the CamKIIα promoter (45). We transfected individual spheroids in a 96-multiwell plate with 0.5 μl 7 to 10 days before each recording. The spheroid is transferred into a multifunctional 3D MEA with integrated blue μ-ILED lights for optical stimulation experiments.

Schemes for HSP assay

Focal heating involved delivery of 52 mW of electrical power across the thermal actuator for 1 hour. After 1 hours of focal heat stress, the spheroids were removed from the device and allowed to recover for 24 hours before being fixed with 4% paraformaldehyde for 15 min and then stored in PBS until immunostaining. The fixed spheroids were stained for HSP70/72 (HSP, Enzo, ADI-SPA-812), neurofilament heavy chain (NF, Abcam, ab72996), and DAPI (Invitrogen, D1306) and imaged with confocal microscopy (46, 47).

Procedures for FEA

Analysis and prediction of the nonlinear mechanical behavior of 3D structures under compressive forces induced by the prestretched elastomer substrates used 3D FEA with the commercial software package Abaqus. Eight-node solid elements and four-node shell elements were chosen for the substrates and the 2D/3D structures, respectively. Convergence tests of the mesh size were conducted to ensure computational accuracy. Linear buckling analysis for the 2D precursor structures under compression was performed to determine the critical buckling strain and corresponding buckling mode, which were then considered as initial geometric imperfections in post-buckling simulations. Deformed shapes and strain distributions at different prestrains for the 3D structures together with the substrate were thus obtained. PI and parylene-C were simulated as linear elastic materials with elastic modulus and Poisson's ratio of $E_{PI} = 2.5$ GPa, $\nu_{PI} = 0.34$ and $E_{parylene} = 2.76$ GPa, $\nu_{parylene} = 0.4$,

respectively. Gold (Au) was simulated using an idealized elastoplastic model (without hardening; yield strain chosen as 0.3%). The elastic modulus and Poisson's ratio are $E_{Au} = 78$ GPa and $\nu_{Au} = 0.44$. The cortical spheroid was modeled as an incompressible solid material with an elastic modulus of ~1 kPa (48, 49). The substrate material (PDMS, 20:1) was modeled as an incompressible Mooney-Rivlin solid, with an elastic modulus of $E_{substrate} = 0.7$ MPa (50).

Optical simulations by Monte Carlo methods

Light propagation in aqueous environment and organoid stimulation was phenomenologically modeled using the Monte Carlo simulation technique (51). The optical stimulation involved a blue (470-nm center emission wavelength) μ-ILED illuminating the surrounding medium with an optical power of 6.1 mW and 120° full divergence angle. The numerical volume was divided in $500 \times 500 \times 500$ bins each of 0.01 mm^3 volume. A total of 3.1×10^6 photons was launched into the numerical volume from a 0.22 mm $\times 0.27$ mm square area corresponding to the active emission area of the μ-ILED. The absorption of water at the wavelength of interest is $\mu_a = 0.0001$ cm^{-1} (52). The scattering and anisotropy factor were set at $\mu_s = 1$ cm^{-1} and $g = 0.9$, respectively. The numerical results describing the photon fluence were exported to Paraview 5.7.0 to render the illumination profile observed as irradiance iso-contours of 1, 2, 5, and 10 mW/mm^2; see Fig. 5E (53). Furthermore, the irradiance along the direct line of sight between the μ-ILED and the centroid of the organoid (see fig. S16F) was extracted, showing the irradiance decay (fig. S16E).

Simulations of thermal physics by FEA

The 3D heat transfer physics simulations used the commercial software COMSOL Multiphysics to simulate both the solid materials (i.e., heater, PDMS substrate, and spheroid) and the surrounding fluids (culture solution). The geometries with detailed parameters are shown in Fig. 5F. Free tetrahedral mesh generated by default physics-controlled method with predefined finer element size was used, and quadratic Lagrange discretization method of temperature ensured sufficient accuracy. The environmental temperature at the outer boundary was set to be 35°C, and the heat source was set with a fixed heat rate of 38 mW.

SUPPLEMENTARY MATERIALS

Supplementary material for this article is available at http://advances.sciencemag.org/cgi/content/full/7/12/eabf9153/DC1

REFERENCES AND NOTES

1. M. A. Lancaster, M. Renner, C.-A. Martin, D. Wenzel, L. S. Bicknell, M. E. Hurles, T. Homfray, J. M. Penninger, A. P. Jackson, J. A. Knoblich, Cerebral organoids model human brain development and microcephaly. *Nature* **501**, 373–379 (2013).
2. A. M. Paşca, S. A. Sloan, L. E. Clarke, Y. Tian, C. D. Makinson, N. Huber, C. H. Kim, J.-Y. Park, N. A. O'Rourke, K. D. Nguyen, S. J. Smith, J. R. Huguenard, D. H. Geschwind, B. A. Barres, S. P. Paşca, Functional cortical neurons and astrocytes from human pluripotent stem cells in 3D culture. *Nat. Methods* **12**, 671–678 (2015).
3. M. A. Lancaster, N. S. Corsini, S. Wolfinger, E. H. Gustafson, A. W. Phillips, T. R. Burkard, T. Otani, F. J. Livesey, J. A. Knoblich, Guided self-organization and cortical plate formation in human brain organoids. *Nat. Biotechnol.* **35**, 659–666 (2017).
4. D. Huh, G. A. Hamilton, D. E. Ingber, From 3D cell culture to organs-on-chips. *Trends Cell Biol.* **21**, 745–754 (2011).
5. H. Clevers, Modeling development and disease with organoids. *Cell* **165**, 1586–1597 (2016).
6. M. A. Lancaster, J. A. Knoblich, Organogenesis in a dish: Modeling development and disease using organoid technologies. *Science* **345**, 1247125 (2014).
7. B. Koo, B. Choi, H. Park, K.-J. Yoon, Past, present, and future of brain organoid technology. *Mol. Cells* **42**, 617–627 (2019).
8. M. A. Lancaster, Brain organoids get vascularized. *Nat. Biotechnol.* **36**, 407–408 (2018).
9. C. A. Trujillo, R. Gao, P. D. Negraes, J. Gu, J. Buchanan, S. Preissl, A. Wang, W. Wu, G. G. Haddad, I. A. Chaim, A. Domissy, M. Vandenberghe, A. Devor, G. W. Yeo, B. Voytek, A. R. Muotri, Complex oscillatory waves emerging from cortical organoids model early human brain network development. *Cell Stem Cell* **25**, 558–569.e7 (2019).
10. T.-W. Chen, T. J. Wardill, Y. Sun, S. R. Pulver, S. L. Renninger, A. Baohan, E. R. Schreiter, R. A. Kerr, M. B. Orger, V. Jayaraman, L. L. Looger, K. Svoboda, D. S. Kim, Ultrasensitive fluorescent proteins for imaging neuronal activity. *Nature* **499**, 295–300 (2013).
11. T. Patriarchi, J. R. Cho, K. Merten, A. Marley, G. J. Broussard, R. Liang, J. Williams, A. Nimmerjahn, M. von Zastrow, V. Gradinaru, L. Tian, Imaging neuromodulators with high spatiotemporal resolution using genetically encoded indicators. *Nat. Protoc.* **14**, 3471–3505 (2019).
12. C. Grienberger, A. Konnerth, Imaging calcium in neurons. *Neuron* **73**, 862–885 (2012).
13. J. Cools, Q. Jin, E. Yoon, D. A. Burbano, Z. Luo, D. Cuypers, G. Callewaert, D. Braeken, D. H. Gracias, A micropatterned multielectrode shell for 3D spatiotemporal recording from live cells. *Adv. Sci.* **5**, 1700731 (2018).
14. A. Kalmykov, C. Huang, J. Bliley, D. Shiwarski, J. Tashman, A. Abdullah, S. K. Rastogi, S. Shukla, E. Mataev, A. W. Feinberg, K. J. Hsia, T. Cohen-Karni, Organ-on-e-chip: Three-dimensional self-rolled biosensor array for electrical interrogations of human electrogenic spheroids. *Sci. Adv.* **5**, eaax0729 (2019).
15. B. H. Kim, F. Liu, Y. Yu, H. Jang, Z. Xie, K. Li, J. Lee, J. Y. Jeong, A. Ryu, Y. Lee, D. H. Kim, X. Wang, K. H. Lee, J. Y. Lee, S. M. Won, N. Oh, J. Kim, J. Y. Kim, S.-J. Jeong, K.-I. Jang, S. Lee, Y. Huang, Y. Zhang, J. A. Rogers, Mechanically guided post-assembly of 3D electronic systems. *Adv. Funct. Mater.* **28**, 1803149 (2018).
16. S. Xu, Z. Yan, K.-I. Jang, W. Huang, H. Fu, J. Kim, Z. Wei, M. Flavin, J. M. Cracken, R. Wang, A. Badea, Y. Liu, D. Xiao, G. Zhou, J. Lee, H. U. Chung, H. Cheng, W. Ren, A. Banks, X. Li, U. Paik, R. G. Nuzzo, Y. Huang, Y. Zhang, J. A. Rogers, Assembly of micro/nanomaterials into complex, three-dimensional a by compressive buckling. *Science* **347**, 154–159 (2015).
17. Y. Park, H. Luan, K. Kwon, S. Zhao, D. Franklin, H. Wang, H. Zhao, W. Bai, J. U. Kim, W. Lu, J.-H. Kim, Y. Huang, Y. Zhang, J. A. Rogers, Transformable, freestanding 3D mesostructures based on transient materials and mechanical interlocking. *Adv. Funct. Mater.* **29**, 1903181 (2019).
18. L. Valentini, S. Bittolo Bon, L. Mussolin, N. M. Pugno, Silkworm silk fibers vs PEEK reinforced rubber luminescent strain gauge and stretchable composites. *Compos. Sci. Technol.* **156**, 254–261 (2018).
19. M. C. N. Marchetto, C. Carromeu, A. Acab, D. Yu, G. W. Yeo, Y. Mu, G. Chen, F. H. Gage, A. R. Muotri, A model for neural development and treatment of rett syndrome using human induced pluripotent stem cells. *Cell* **143**, 527–539 (2010).
20. N. Gunhanlar, G. Shpak, M. van der Kroeg, L. A. Gouty-Colomer, S. T. Munshi, B. Lendemeijer, M. Ghazvini, C. Dupont, W. J. G. Hoogendijk, J. Gribnau, F. M. S. de Vrij, S. A. Kushner, A simplified protocol for differentiation of electrophysiologically mature neuronal networks from human induced pluripotent stem cells. *Mol. Psychiatry* **23**, 1336–1344 (2017).
21. O. Sirenko, F. Parham, S. Dea, N. Sodhi, S. Biesmans, S. Mora-Castilla, K. Ryan, M. Behl, G. Chandy, C. Crittenden, S. Vargas-Hurlston, O. Guicherit, R. Gordon, F. Zanella, C. Carromeu, Functional and mechanistic neurotoxicity profiling using human iPSC-Derived neural 3D cultures. *Toxicol. Sci.* **167**, 58–76 (2019).
22. L. Zhang, M. Wei, L. Shao, M. Li, W. Dai, Y. Cui, Z. Li, C. Zhang, W. Wang, Enhanced parylene-C fluorescence as a visual marker for neuronal electrophysiology applications. *Lab Chip* **18**, 3539–3549 (2018).
23. A. Kepecs, X. J. Wang, Analysis of complex bursting in cortical pyramidal neuron models. *Neurocomputing.* **32–33**, 181–187 (2000).
24. D. S. Bassett, O. Sporns, Network neuroscience. *Nat. Neurosci.* **20**, 353–364 (2017).
25. F. Birey, J. Andersen, C. D. Makinson, S. Islam, W. Wei, N. Huber, H. C. Fan, K. R. Cordes Metzler, G. Panagiotakos, N. Thom, N. A. O'Rourke, L. M. Steinmetz, J. A. Bernstein, J. Hallmayer, J. R. Huguenard, S. P. Paşca, Assembly of functionally integrated human forebrain spheroids. *Nature* **545**, 54–59 (2017).
26. J. A. Bagley, D. Reumann, S. Bian, J. Lévi-Strauss, J. A. Knoblich, Fused cerebral organoids model interactions between brain regions. *Nat. Methods* **14**, 743–751 (2017).
27. S. P. Pasca, Assembling human brain organoids. *Science* **363**, 126–127 (2019).
28. S. M. Won, E. Song, J. T. Reeder, J. A. Rogers, Emerging modalities and implantable technologies for neuromodulation. *Cell* **181**, 115–135 (2020).
29. S. Luan, I. Williams, K. Nikolic, T. G. Constandinou, Neuromodulation: Present and emerging methods. *Front. Neuroeng.* **7**, 27 (2014).
30. E. Dayan, N. Censor, E. R. Buch, M. Sandrini, L. G. Cohen, Noninvasive brain stimulation: From physiology to network dynamics and back. *Nat. Neurosci.* **16**, 838–844 (2013).
31. D.-W. Park, J. P. Ness, S. K. Brodnick, C. Esquibel, J. Novello, F. Atry, D.-H. Baek, H. Kim, J. Bong, K. I. Swanson, A. J. Suminski, K. J. Otto, R. Pashaie, J. C. Williams, Z. Ma, Electrical

neural stimulation and simultaneous *in vivo* monitoring with transparent graphene electrode arrays implanted in GCaMP6f mice. *ACS Nano* **12**, 148–157 (2018).

32. S. Ahn, S. Jo, S. B. Jun, H. W. Lee, S. Lee, Prediction of the seizure suppression effect by electrical stimulation via a computational modeling approach. *Front. Comput. Neurosci.* **11**, 39 (2017).

33. O. Yizhar, L. E. Fenno, M. Prigge, F. Schneider, T. J. Davidson, D. J. O'Shea, V. S. Sohal, I. Goshen, J. Finkelstein, J. T. Paz, K. Stehfest, R. Fudim, C. Ramakrishnan, J. R. Huguenard, P. Hegemann, K. Deisseroth, Neocortical excitation/inhibition balance in information processing and social dysfunction. *Nature* **477**, 171–178 (2011).

34. E. L. Reilly, B. Barlogie, M. A. Seward, P. M. Corry, B. Rigor, E. Yip, Persistence of EEG activity with prolonged induced hyperthermic fever. *Clin. Electroencephalogr.* **11**, 22–27 (1980).

35. M. Horowitz, S. D. M. Robinson, Heat shock proteins and the heat shock response during hyperthermia and its modulation by altered physiological conditions. *Prog. Brain Res.* **162**, 433–446 (2007).

36. E. E. Benarroch, Heat shock proteins: Multiple neuroprotective functions and implications for neurologic disease. *Neurology* **76**, 660–667 (2011).

37. F. R. Cugola, I. R. Fernandes, F. B. Russo, B. C. Freitas, J. L. M. Dias, K. P. Guimarães, C. Benazzato, N. Almeida, G. C. Pignatari, S. Romero, C. M. Polonio, I. Cunha, C. L. Freitas, W. N. Brandão, C. Rossato, D. G. Andrade, D. D. P. Faria, A. T. Garcez, C. A. Buchpigel, C. T. Braconi, E. Mendes, A. A. Sall, P. M. D. A. Zanotto, J. P. S. Peron, A. R. Muotri, P. C. B. B. Beltrao-Braga, The Brazilian Zika virus strain causes birth defects in experimental models. *Nature* **534**, 267–271 (2016).

38. P. P. Garcez, E. C. Loiola, R. M. da Costa, L. M. Higa, P. Trindade, R. Delvecchio, J. M. Nascimento, R. Brindeiro, A. Tanuri, S. K. Rehen, Zika virus impairs growth in human neurospheres and brain organoids. *Science* **352**, 816–818 (2016).

39. X. Qian, H. N. Nguyen, M. M. Song, C. Hadiono, S. C. Ogden, C. Hammack, B. Yao, G. R. Hamersky, F. Jacob, C. Zhong, K.-J. Yoon, W. Jeang, L. Lin, Y. Li, J. Thakor, D. A. Berg, C. Zhang, E. Kang, M. Chickering, D. Nauen, C.-Y. Ho, Z. Wen, K. M. Christian, P.-Y. Shi, B. J. Maher, H. Wu, P. Jin, H. Tang, H. Song, G.-L. Ming, Brain-region-specific organoids using mini-bioreactors for modeling ZIKV exposure. *Cell* **165**, 1238–1254 (2016).

40. H. Kim, H. J. Park, H. Choi, Y. Chang, H. Park, J. Shin, J. Kim, C. J. Lengner, Y. K. Lee, J. Kim, Modeling G2019S-LRRK2 sporadic Parkinson's disease in 3D midbrain organoids. *Stem Cell Reports.* **12**, 518–531 (2019).

41. D. M. Cairns, N. Rouleau, R. N. Parker, K. G. Walsh, L. Gehrke, D. L. Kaplan, A 3D human brain–like tissue model of herpes-induced Alzheimer's disease. *Sci. Adv.* **6**, eaay8828 (2020).

42. Y. Xiang, Y. Tanaka, B. Patterson, Y.-J. Kang, G. Govindaiah, N. Roselaar, B. Cakir, K.-Y. Kim, A. P. Lombroso, S.-M. Hwang, M. Zhong, E. G. Stanley, A. G. Elefanty, J. R. Naegele, S.-H. Lee, S. M. Weissman, I.-H. Park, Fusion of regionally specified hPSC-derived organoids models human brain development and interneuron migration. *Cell Stem Cell* **21**, 383–398.e7 (2017).

43. J. Jo, Y. Xiao, A. X. Sun, E. Cukuroglu, H.-D. Tran, J. Göke, Z. Y. Tan, T. Y. Saw, C.-P. Tan, H. Lokman, Y. Lee, D. Kim, H. S. Ko, S.-O. Kim, J. H. Park, N.-J. Cho, T. M. Hyde, J. E. Kleinman, J. H. Shin, D. R. Weinberger, E. K. Tan, H. S. Je, H.-H. Ng, Midbrain-like organoids from human pluripotent stem cells contain functional dopaminergic and neuromelanin-producing neurons. *Cell Stem Cell* **19**, 248–257 (2016).

44. C. Bardy, M. van den Hurk, T. Eames, C. Marchand, R. V. Hernandez, M. Kellogg, M. Gorris, B. Galet, V. Palomares, J. Brown, A. G. Bang, J. Mertens, L. Böhnke, L. Boyer, S. Simon, F. H. Gage, Neuronal medium that supports basic synaptic functions and activity of human neurons in vitro. *Proc. Natl. Acad. Sci. U.S.A.* **112**, E2725–E2734 (2015).

45. D. R. Hochbaum, Y. Zhao, S. L. Farhi, N. Klapoetke, C. A. Werley, V. Kapoor, P. Zou, J. M. Kralj, D. Maclaurin, N. Smedemark-Margulies, J. L. Saulnier, G. L. Boulting, C. Straub, Y. K. Cho, M. Melkonian, G. K.-S. Wong, D. J. Harrison, V. N. Murthy, B. L. Sabatini, E. S. Boyden, R. E. Campbell, A. E. Cohen, All-optical electrophysiology in mammalian neurons using engineered microbial rhodopsins. *Nat. Methods* **11**, 825–833 (2014).

46. D. Lavinsky, J. Wang, P. Huie, R. Dalal, S. J. Lee, D. Y. Lee, D. Palanker, Nondamaging retinal laser therapy: Rationale and applications to the macula. *Investig. Ophthalmol. Vis. Sci.* **57**, 2488–2500 (2016).

47. M. Locke, C. Celotti, The effect of heat stress on skeletal muscle contractile properties. *Cell Stress Chaperones* **19**, 519–527 (2014).

48. A. Gefen, S. S. Margulies, Are in vivo and in situ brain tissues mechanically similar? *J. Biomech.* **37**, 1339–1352 (2004).

49. N. D. Leipzig, M. S. Shoichet, The effect of substrate stiffness on adult neural stem cell behavior. *Biomaterials* **30**, 6867–6878 (2009).

50. P. H. Niewiarowski, A. Y. Stark, A. Dhinojwala, Biological microstructures with enhanced adhesion and friction: A numerical approach structured adhesives. (Springer, New York, 2017), pp.141–178.

51. L. Wang, S. L. Jacques, L. Zheng, MCML––Monte Carlo modeling of light transport in multi-layered tissues. *Comput. Methods Programs Biomed.* **47**, 131–146 (1995).

52. R. M. Pope, E. S. Fry, Absorption spectrum (380–700 nm) of pure water II Integrating cavity measurements. *Appl. Optics* **36**, 8710–8723 (1997).

53. J. Ahrens, B. Geveci, C. Law, in *Visualization Handbook* (Elsevier, 2005), pp. 717–731.

Science Advances

Three-dimensional, multifunctional neural interfaces for cortical spheroids and engineered assembloids

Yoonseok Park, Colin K. Franz, Hanjun Ryu, Haiwen Luan, Kristen Y. Cotton, Jong Uk Kim, Ted S. Chung, Shiwei Zhao, Abraham Vazquez-Guardado, Da Som Yang, Kan Li, Raudel Avila, Jack K. Phillips, Maria J. Quezada, Hokyung Jang, Sung Soo Kwak, Sang Min Won, Kyeongha Kwon, Hyoyoung Jeong, Amay J. Bandodkar, Mengdi Han, Hangbo Zhao, Gabrielle R. Osher, Heling Wang, KunHyuck Lee, Yihui Zhang, Yonggang Huang, John D. Finan and John A. Rogers

ARTICLE TOOLS	http://advances.sciencemag.org/content/7/12/eabf9153
SUPPLEMENTARY MATERIALS	http://advances.sciencemag.org/content/suppl/2021/03/15/7.12.eabf9153.DC1
REFERENCES	This article cites 51 articles, 7 of which you can access for free http://advances.sciencemag.org/content/7/12/eabf9153#BIBL
PERMISSIONS	http://www.sciencemag.org/help/reprints-and-permissions

Use of this article is subject to the Terms of Service